Conformational diversity of dynactin sidearm and domain organization of its subunit p150

Kei Saito[a,†], Takashi Murayama[b,†], Tomone Hata[a], Takuya Kobayashi[b], Keitaro Shibata[a,‡], Saiko Kazuno[c], Tsutomu Fujimura[c,§], Takashi Sakurai[b], and Yoko Y. Toyoshima[a,d,*]

[a]Department of Life Sciences, Graduate School of Arts and Sciences and [d]Komaba Institute for Science, Graduate School of Arts and Sciences, The University of Tokyo, Meguro-ku, Tokyo 153-8902, Japan; [b]Department of Cellular and Molecular Pharmacology and [c]Laboratory of Proteomics and Biomolecular Science, Biomedical Research Center, Juntendo University Graduate School of Medicine, Bunkyo-ku, Tokyo 113-8421, Japan

ABSTRACT **Dynactin is a principal regulator of the minus-end directed microtubule motor dynein. The sidearm of dynactin is essential for binding to microtubules and regulation of dynein activity. Although our understanding of the structure of the dynactin backbone (Arp1 rod) has greatly improved recently, structural details of the sidearm subcomplex remain elusive. Here, we report the flexible nature and diverse conformations of dynactin sidearm observed by electron microscopy. Using nanogold labeling and deletion mutant analysis, we determined the domain organization of the largest subunit p150 and discovered that its coiled-coil (CC1), dynein-binding domain, adopted either a folded or an extended form. Furthermore, the entire sidearm exhibited several characteristic forms, and the equilibrium among them depended on salt concentrations. These conformational diversities of the dynactin complex provide clues to understanding how it binds to microtubules and regulates dynein.**

Monitoring Editor
Thomas Surrey
Francis Crick Institute

Received: Jan 16, 2020
Revised: Mar 23, 2020
Accepted: Mar 27, 2020

INTRODUCTION

Dynactin is a multisubunit complex that plays many essential roles in various cell functions, especially as an adaptor of dynein to vesicles or organelles (Schroer, 2004; Kardon and Vale, 2009). The importance of dynactin as a principal regulator of dynein and as an organizer of microtubule-based traffic is established, but the molecular mechanisms of its diverse functions are not well understood mainly because of its very large and complicated architecture.

The dynactin complex is almost as large (~1.2 MDa) as cytoplasmic dynein and is composed of 11 different subunits (Schroer, 2004; Carter *et al.*, 2016). This complex forms a unique asymmetric structure comprising two distinct domains, the Arp1 rod and the sidearm (Eckley *et al.*, 1999). The Arp1 rod consists primarily of a polymer of Arp1 (Hodgkinson *et al.*, 2005; Imai *et al.*, 2006) and is responsible for cargo binding. One end of the rod (called the pointed-end) is capped by the "pointed-end complex" which consists of Arp11, p25, p27, and p62 (Eckley *et al.*, 1999; Zhang *et al.*, 2011; Yeh *et al.*, 2012, 2013), whereas the other end (called the barbed end) is capped by CapZ α/β (Schafer *et al.*, 1994).

The sidearm is a thin, elongated structure projecting from the barbed end of the Arp1 rod. The main constituent of the sidearm is a dimer of p150^{Glued} (hereafter referred to as p150). It interacts with dynein (Karki and Holzbaur, 1995; Vaughan and Vallee, 1995) and microtubules (Waterman-Storer *et al.*, 1995), and numerous mutations in DCTN1 (the gene encoding p150) have been reported to cause neurodegenerative diseases (Konno *et al.*, 2017). p150 is composed of functionally and structurally distinctive domains. N-terminal region of p150 contains CAP-Gly and the basic amino acid-rich domains, both of which are responsible for MT binding. CAP-Gly is a small globular protein module, which is included in some members of +TIPs (Steinmetz and Akhmanova, 2008). The basic amino acid-rich domain supports MT binding (Culver-Hanlon *et al.*, 2006; Kobayashi *et al.*, 2006; Wang *et al.*, 2014) and the majority of it is intrinsically disordered (Guo *et al.*, 2019). p150 is predicted to

This article was published online ahead of print in MBoC in Press (http://www.molbiolcell.org/cgi/doi/10.1091/mbc.E20-01-0031) on April 2, 2020.

†These authors contributed equally to this work.

Present addresses: ‡Advanced ICT Research Institute, National Institute of Information and Communications Technology, Kobe, Hyogo, Japan; §Laboratory of Bioanalytical Chemistry, Tohoku Medical and Pharmaceutical University, Miyagi, Japan.

*Address correspondence to: Yoko Y. Toyoshima (cyytoyo@mail.ecc.u-tokyo.ac.jp).

Abbreviations used: aa, amino acid; CC1, coiled coil 1; CC2, coiled coil 2; EM, electron microscopy; GFP-N, GFP and N-region; His-tag, octa-histidine tag; ICD, inter-coiled-coil domain; SBP, streptavidin-binding peptide.

have a long (~330 amino acids [aa]) coiled-coil domain (CC1) following the MT-binding region and to have another coiled-coil (CC2; ~130 aa) on the C-terminal side. CC1 interacts with dynein (Miura *et al.*, 2010; King *et al.*, 2003; Kobayashi *et al.*, 2017).

The proximal end of the sidearm is called the "shoulder." This domain is composed of some part of p150, four copies of p50 (also called dynamitin), and two copies of p24 (Eckley *et al.*, 1999). The shoulder is considered to be essential for tethering the sidearm to the Arp1 rod because overexpression of p50 disrupts the interaction between the sidearm and the rod (Echeverri *et al.*, 1996; Melkonian *et al.*, 2007; Maier *et al.*, 2008; Jacquot *et al.*, 2010).

Recently, a cryo-electron microscopy (EM) study (Urnavicius *et al.*, 2015) revealed the detailed structure of the dynactin complex. The rigid backbone of the complex including the Arp1 rod and the shoulder domain was especially well resolved. In contrast, the distal part of the sidearm, corresponding to p150, was observed only under conditions where p150 was docked to the Arp1 rod. This configuration is markedly different from previously observed deep-etch rotary shadowing EM images of the dynactin complex (Schafer *et al.*, 1994) (Figure 1A). In addition, p150 has scarcely been observed in other 2D or 3D averaged data of dynactin complex (Hodgkinson *et al.*, 2005; Imai *et al.*, 2006, 2014; Chowdhury *et al.*, 2015). This elusiveness of p150 is likely derived from the flexible nature of the protein, which makes it difficult to properly understand the structure–function relationship of the dynactin complex, especially the mechanical basis for the dynamic interaction of dynactin with dynein and MTs.

CC1 is a particularly intriguing domain of p150 since, despite its well-known biochemical characteristic as the dynein-binding domain (King *et al.*, 2003; Morgan *et al.*, 2011), its structure and function remain controversial. CC1 was previously proposed to be located along the sidearm and the Arp1 rod (Schroer, 2004). A recent cryo-EM study assigned CC1 to the structure extending from the head domain (Urnavicius *et al.*, 2015). The study suggested that CC1 folds back at the distal end of the sidearm, which might correspond to the second projection occasionally observed in the rotary shadowing EM (Schafer *et al.*, 1994). However, the docked configuration in the cryo-EM left some important physiological questions unsolved. For example, which configuration does dynactin take in the cell and could CC1 adopt an extended conformation when dynactin binds to MTs or dynein, as postulated by Cianfrocco *et al.* (2015) or Carter *et al.* (2016)? Furthermore, the results of in vitro assays that examined the effect of CC1 on dynein motility were conflicting: the effect was negative (Tripathy *et al.*, 2014; Kobayashi *et al.*, 2017), not significant (Culver-Hanlon *et al.*, 2006; Ayloo *et al.*, 2014), or positive (Kardon *et al.*, 2009). Possibly, there exist some regulatory mechanisms within CC1. Considering its structural and functional complexity, determining the location and conformation of CC1 in the dynactin complex, when it is not averaged and not docked, may be a key to understanding dynactin in action.

Here, by combining negative stain EM and site-directed nanogold labeling (Kitai *et al.*, 2011), we identified all domains in p150 without averaging. In our "nonaveraged" observations of individual molecules, the sidearm was remarkably flexible and adopted various morphologies. Notably, CC1 exhibited two forms, a folded form and an extended form, suggesting that CC1 undergoes a large conformational change. Furthermore, with the aid of 2D single particle analysis, conformations of the entire sidearm were classified into several characteristic forms and some of those were proven to be in equilibrium. We propose a new model of the dynactin sidearm with multiple conformations and discuss how intramolecular interaction within the dynactin complex regulates its ability to bind to microtubules and dynein.

RESULTS

EM observation of the dynactin complex revealed the flexibility of the "undocked" sidearm

We purified the human recombinant dynactin complex for EM observation. A streptavidin binding peptide (SBP) was fused to one of the subunits (Supplemental Figure S1[1]) and all the other subunit components of the dynactin complex were successfully copurified by affinity chromatography (Supplemental Figure S1[2]). We first used a complex including recombinant p62 (SBP-p62 in Supplemental Figure S1[1]), which is known to be located at the pointed end of the Arp1 rod (Schafer *et al.*, 1994; Kitai *et al.*, 2011), to investigate the structure of the native dynactin sidearm. The negative stain EM images revealed the sidearm complex projecting from one end of the Arp1 rod (Figure 1B; Supplemental Figure S1[3A]). The overall configuration of the sidearm and the orientation of the projection were remarkably diverse, implying the flexible nature of the sidearm. Nevertheless, the sidearm exhibited the following common morphological features among individual molecules: it contained a "shoulder" at the proximal part (closer to the Arp1 rod), a "head" composed of two globular masses at the distal part, and a filamentous "neck" in the middle (Figure 1B, bottom right cartoon). We designated the reference points based on these structural signatures (Supplemental Figure S1[3B]) and described the geometry of the sidearm, which probably reflected its range of motion (Supplemental Figure 1[3C]).

The morphological characteristics of the sidearm were similar to those of native chick dynactin revealed by deep-etch rotary shadowing EM (Schafer *et al.*, 1994) in its overall configuration and flexibility as well as in the size and appearance of each domain, indicating that our recombinant approach retained the structural integrity of the dynactin complex. Under our experimental conditions, the majority of the molecules exhibited an "undocked" sidearm; the sidearm did not dock to the Arp1 rod (Figure 1, Ba–Bh). Meanwhile, molecules resembling the cryo-EM images (Urnavicius *et al.*, 2015), in which the sidearm docked to or crossed the Arp1 rod, were rarely observed (Figure 1, Bi and Bj).

On closer examination of the proximal part of undocked sidearm, it was found that the shoulder domain was docked in some molecules (shoulder-docked form; Figure 1, Be–Bh) but not in others (shoulder-undocked form; Figure 1, Ba–Bd). To classify the molecules, EM images were processed by 2D single particle analysis. Particles were aligned and classified by the Arp1 rod, and then by both the Arp1 rod and the shoulder (Supplemental Figure S1[4]). Expectedly, the analysis generated classes corresponding to the shoulder-undocked form (Figure 1C) and the shoulder-docked form (Figure 1D). The Arp1 rod was rather homogenous, whereas the position of the head was so widely scattered that it was blurred in the averaged images (Figure 1, C and D; Supplemental Figure S1[4, bottom]). Homogeneity/heterogeneity of the shoulder domain was varied depending on classes. The averaged structural image of the shoulder was clearly obtained only in the shoulder-docked form (Figure 1D) but was otherwise blurred (Figure 1C; Supplemental Figure S1[4, bottom]). Importantly, the head moved throughout a broad area even when the shoulder was docked (Figure 1D, green; Supplemental Figure S1[3D]). Furthermore, it was occasionally positioned at the other side of the Arp1 rod, that is, the neck crossed the rod (Figure 1D, bottom right panel and dashed frame in top right). Note that we do not regard this form, corresponding to i and j in Figure 1B, as identical to the docked form reported in the cryo-EM study because the position of the head was not fixed under our current conditions. Taken together, these results demonstrate that the sidearm is highly flexible as a whole and that the mobility of

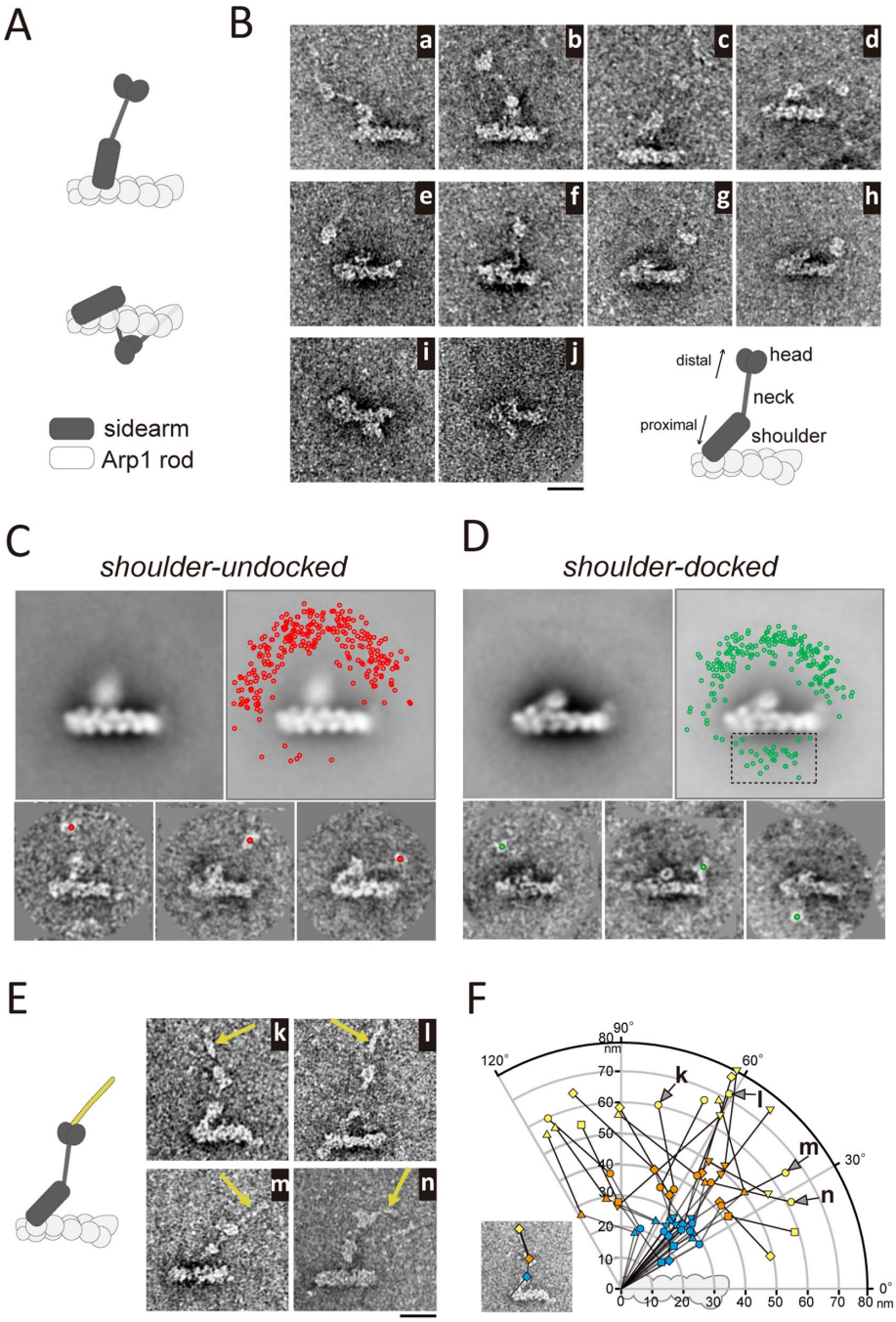

FIGURE 1: Dynactin sidearm exhibits diverse morphologies with a filament at its distal end. (A) Models of dynactin complex structure. Light gray, Arp1 rod; dark gray, sidearm. Top, based on Schafer *et al.* (1994) and Schroer (2004); bottom, based on Urnavicius *et al.* (2015). (B) Negative stain EM images of the dynactin complexes (SBP-p62) with a cartoon to illustrate each part of the dynactin sidearm (bottom right). A gallery shows diverse morphologies of the sidearm: (a–d) the shoulder-undocked form; (e–h) the shoulder-docked form with the neck not crossing the Arp1 rod; (i, j) the shoulder-docked form with the neck crossing the Arp1 rod. (C) The shoulder-undocked sidearm classified by single particle analysis. See Supplemental Figure S1(4) for details of image processing. Top left, averaged image of the class. Top right, distribution of the head positions of molecules in the class (red dots, $N = 265$) superimposed on the averaged image (whose transparency was modulated). The head position of each molecule in the aligned stack was obtained by thresholding and centroid measurement using ImageJ software. Bottom, representative images of the class. Red dots indicate the positions of the heads. See Figure 5, A and B and Supplemental Figure S5(1) for analysis of the shoulder domain. (D) The shoulder-docked sidearm classified by single particle analysis (class III in Supplemental Figure S1[4]). The layout is the same as C. Green dots indicate the positions of the heads ($N = 235$). The green dots in the dashed frame in the top right image indicate the head positions of the molecules in which the neck domain crosses the Arp1 rod. (E) EM images of the dynactin complex with the distinctive distal filament (yellow arrows). (F) Geometry of the sidearms with the distal filament. The polar coordinates of the shoulder–neck junction (light blue), head (orange), and the tip of the distal filament (yellow) were measured with the origin located at the barbed end of the Arp1 rod. The molecules with distinctive distal filament ($N = 20$) are taken from the data set shown in Supplemental Figure S1(3F). Each polygonal line indicates the backbone of the sidearm of each molecule. The positions of the distal filament (X-W in Supplemental Figure S1[3F]) are indicated by bold lines and those of other parts in the sidearm (X-Y-P in Supplemental Figure S1[3F]) by thin lines. To help distinguish among molecules, the sets of colored plots are marked with several symbols (circle, triangle up, triangle down, square, diamond). The plots labeled k–n correspond to the molecules shown in E, and the EM image of k is shown here again as an example of the measurement. Bars represent 20 nm.

the neck-shoulder junction (Supplemental Figure S1[3B, point Y]) is sufficient for the head and the other distal part of the sidearm to move around.

Thin filamentous structure was observed at the distal sidearm

On inspection of the head domain, we noticed a thin filamentous structure, which was located distal to the heads (Figure 1E, yellow arrows; Supplemental Figure S1[3E]). This structure was particularly subtle compared with other parts of the dynactin complex and its visibility was rather varied even on the same grid; the ratio of the dynactin complex with such a thin filamentous structure in the appropriately stained region was 40–45% ($N = 245$, two independent experiments). The continuity between this structure and the two globular heads was not always clear, possibly because it had a particularly thin structure. Nonetheless, since it was found in almost every construct examined with similar appearance and since mass spectrometry analysis of the purified sample detected no proteins known for binding with p150 (Supplemental Table S1), we assume that this filament was a part of the dynactin sidearm located at the very distal part (Figure 1E, left cartoon) but was not always visible by negative stain EM. The distal filament also pointed in a wide range of angles (Figure 1F). The distance between the tip of the filament and the center of the head was 28.8 ± 4.1 nm (mean ± SD,

$N = 20$); the "somatometry" of the dynactin complex is summarized in Supplemental Figure S1(3F).

A structure similar to the distal filament was observed in the deep-etch rotary shadowed images ("a second projection" in Schafer *et al.*, 1994) but it was not visualized in the previous negative stain EM observations probably because its visibility was susceptible to solution and/or staining conditions (Imai *et al.*, 2006, 2014; Chowdhury *et al.*, 2015). In addition, the structure assigned as a part of p150 (CC1) in the cryo-EM study (Urnavicius *et al.*, 2015) is probably identical to our structure; however, direct comparison is hindered by the fact that it was averaged only when docked to the Arp1 rod. Thus, the identification and further characterization of the sidearm including the distal filament was addressed below.

Domain organization of the p150 subunit in the sidearm

To dissect the molecular architecture of the dynactin sidearm, we made a series of His-tagged mutants of p150 (Supplemental Figure S1[1]) and labeled the tagged site in the dynactin complex with gold nanoparticles modified with Ni-NTA (see *Materials and Methods*). p150 is a large protein (~1250 aa) predicted to form two long coiled-coil structures (CC1 ~50 nm, CC2 ~20 nm) and CC1 has a break in its coiled-coil structure at the hinge point (Figure 2A). p150 mutants carry the His-tag at respective locations: the N- and C-termini of p150, both ends and the hinge of CC1, and both ends of CC2 (Figure 2A; Supplemental Figure S1[1]). The efficiency and specificity of nanogold labeling of dynactin used in this study was similar to those of our previous report (Kitai *et al.*, 2011; Appendix 1).

The nanogold labeling of p150-N-His revealed that the N-terminus of p150 was localized around the head domain (Figure 2B, left). Although the position of each gold nanoparticle was widely scattered, the centroid of the gold nanoparticles was located close to the center of the heads (Supplemental Figure S2[1A]; see also Supplemental Table S2 for statistics of nanogold labeling experiments). For p150-C-His, we found the gold nanoparticles around the shoulder (Figure 2B, right) and measured their distance from the barbed end of the Arp1 rod (Supplemental Figure S2[1B]). These results suggest that p150 is located at the distal part of the sidearm. The location of the N-terminus is consistent with previous models (Schroer, 2004; Urnavicius *et al.*, 2015). The location of the C-terminus does not agree with the model where the C-terminus of p150 extends along the Arp1 rod (Schroer, 2004) but agrees well with the interpretation of cryo-EM data that assigned one of the α-helices seen in the shoulder as p150 C-terminal structure (Urnavicius *et al.*, 2015).

Next, we focused on CC1. CC1 is the longest coiled-coil in p150, the well-known dynein-binding domain, and a supposed constituent of the distal filament (Urnavicius *et al.*, 2015). The nanogold labeling experiments showed that the CC1-start, the starting point of CC1 and the CC1-end, its ending point, were located at the junctions of the head and the filament (Figure 2C, top and bottom). In contrast, the CC1-hinge was located at the tip of the filament (Figure 2C, middle). Mapping of nanogold labeling results also showed that the distribution of the CC1-hinge was broader and more distant from the head than those for the CC1-start and the CC1-end (Figure 2D). We subsequently made a CC1-deletion mutant of p150 (p150 ΔCC1 in Supplemental Figure S1[1]). The distal filament of p150 ΔCC1 was never observed, but the rest of the complex exhibited a configuration similar to that of SBP-p62 including native p150 (Figure 2E, top). The lengths of the shoulder and the neck were almost the same for ΔCC1 and wild-type p150 (Figure 2E, bottom). By nanogold labeling and deletion analysis, we concluded that the distal filament was an essential component of the dynactin sidearm protruding from the head and that it was formed by CC1 of p150 that folded back at the hinge.

The labeling of the second coiled-coil, CC2, showed that CC2-start was located at the head domain and CC2-end at the neck-shoulder junction (i.e., base of the neck) (Figure 2F, left and middle; Supplemental Figure S2[1C and 1D]). In addition, p150 ΔCC2 exhibited a morphology lacking a neck, where the head and the shoulder were in close proximity, and the distal filament formed by CC1 was still evident (Figure 2F, right). These results demonstrated that CC2 was the neck itself.

The observation that both CC1-end and CC2-start were localized at the head domain raised the possibility that the region between CC1 and CC2 constituted a part of the head. This region is rich in helices (Supplemental Figure S2[2A]) and the cryo-EM study assigned this inter-coiled-coil domain (ICD) as the head domain by its mass (Urnavicius *et al.*, 2015). To validate this possibility, we made deletion mutants lacking the entire or a part of ICD (Supplemental Figures S1[1] and S2[2A]). In the mutant lacking the entire ICD (p150 ΔICD), the head domain was almost never observed and the outline of the complex distal to the shoulder domain was quite obscure (Figure 2G, top left; Supplemental Figure S2[2B]). For mutants lacking the former or the latter half of ICD (p150 ΔICD-a and p150 ΔICD-b, respectively), the head domains were more distinct than those of p150 ΔICD (Figure 2G, bottom left and top right; Supplemental Figure S2[2B]), but their head sizes were significantly smaller than that of the wild-type p150 (Supplemental Figure S2[2C]). In all three ICD deletion mutants, the appearance of sidearm structure below the head, namely the neck and shoulder, remained unchanged compared with the wild-type sidearm. In contrast, CC1 was not distinctly observed except for p150 ΔICD-b (Figure 2G, yellow arrows). These results confirm that ICD forms the head domain, or at least a part of it, and the former half (ICD-a) is important for the structural integrity of CC1.

Regarding the constitution of the head domain, we next investigated the contribution of the N-region to the head (Figure 2A). p135 is a spliced isoform of p150 expressed in mammalian neurons that lacks most of the N-region (Tokito *et al.*, 1996; Dixit *et al.*, 2008). Thus, we made two N-region deletion mutants: one mimicking p135 (p135) and the other lacking the entire N-region and starting at CC1 (p150 ΔN) (Supplemental Figure S1[1]). Intriguingly, in these two mutants, the morphology of the sidearm and the size of the head were indistinguishable from those of p150 (Figure 2G, bottom right; Supplemental Figure S2[2, B–D]). Furthermore, CC1 of both p135 and p150 ΔN was observed to be similar to that of wild-type p150 (Figure 2G and Supplemental Figure S2[2D, yellow arrows]). These results suggest that the contribution of the N-region to the size of the head domain may be considerably small in comparison with that of ICD.

Domain organization of p150 revealed by mutant analyses is summarized in Figure 2H. Particularly, the central domains in p150 (CC1, ICD, and CC2) depicted in Figure 2A are now proven to form the body of the distal sidearm (the distal filament, the head, and the neck). Our model is in support of the assignment of the cryo-EM (Urnavicius *et al.*, 2015) in general but there remain important differences (see *Discussion*).

CC1 adopts folded and extended forms

We next focused on how ICD and N-region are structurally linked. CC1 lies between the N-region and ICD and it was occasionally observed to be unfolded (e.g., Figure 1En; Figure 2F, bottom left in p150 ΔCC2 panel) or more extended (Figure 3A) when compared with the ~30 nm protrusion (Supplemental Figure S1[3F]). Here, CC1 was measured to be more than 50 nm in length in some molecules; however, the precise measurement was difficult because the size of

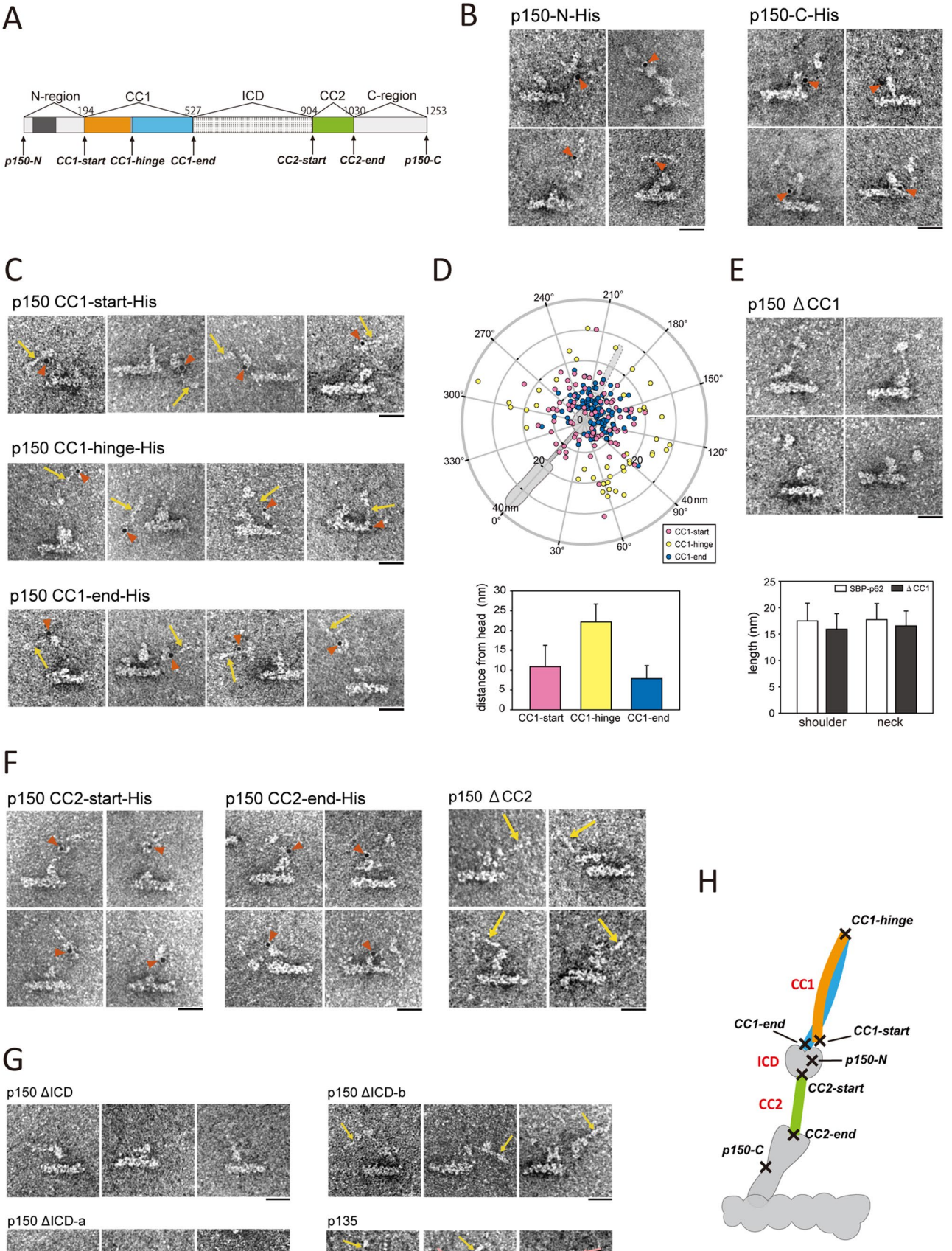
A
N-region
CC1
ICD
CC2
C-region
194
527
904
1030
1253
p150-N
CC1-start
CC1-hinge
CC1-end
CC2-start
CC2-end
p150-C
B
p150-N-His
p150-C-His
C
p150 CC1-start-His
p150 CC1-hinge-His
p150 CC1-end-His
D
CC1-start
CC1-hinge
CC1-end
distance from head (nm)
E
p150 ΔCC1
SBP-p62
ΔCC1
length (nm)
shoulder
neck
F
p150 CC2-start-His
p150 CC2-end-His
p150 ΔCC2
G
p150 ΔICD
p150 ΔICD-b
p150 ΔICD-a
p135
H
CC1-hinge
CC1
CC1-end
CC1-start
ICD
p150-N
CC2-start
CC2
CC2-end
p150-C

the N-region (~190 aa) in wild-type p150 was too small for EM observation. Thus, we fused GFP to the N-terminus of p150 (p150-N-GFP in Supplemental Figure S1[1]) expecting that the mass of the GFP and N-region (GFP-N) should be sufficiently large and detectable under EM. We indeed observed that GFP-N (~490 aa) was as large as ICD (~370 aa) and both domains exhibited similar globular structures. Noticeably, the distance between GFP-N and ICD was varied among molecules (Figure 3, B and C). When GFP and ICD were in close proximity, both structures were seen at the base of CC1 (Figure 3B).

In other cases, however, GFP-N was observed as a separate and distinct domain from ICD, with these two domains bridged by a hooked CC1 (Figure 3C). This finding indicates that CC1 adopts not only a folded form, which was reported in this and previous studies, but also an extended form, which was observed here for the first time. The coexistence of both forms of CC1 in a single sample suggests that CC1 undergoes a conformational change between the two forms. CC1 contains two adjacent parallel coiled-coils, CC1a and CC1b, joined by the hinge and it is likely that they form a supercoil in the folded form, whereas they exist as two separate coiled-coils in the extended form. In line with this, CC1 was thinner in the extended form (Figure 3C) than in the folded form (Figure 3B). Varying visibility of CC1 described above (Figure 1, B and E) may have been derived from the existence of this thinner form of CC1; that is, CC1 may be more difficult to detect by EM in the extended form than in the folded form. When it was visible, CC1 in the extended form exhibited more varied morphologies and was probably more flexible than in the folded form (Figure 3C, Supplemental Figure S3[1]). Furthermore, in some dynactin molecules, the two GFP-N structures were separated from each other (Figure 3C, middle and right; Supplemental Figure S3[1, type 4]). The serine/proline-rich domain (~100 aa) between CAP-Gly and CC1 has recently been shown to be intrinsically disordered (Guo *et al.*, 2019). Thus, we think that the two N-regions in a p150 dimer are able to bifurcate at the N-terminal end of CC1 (CC1-start in Figure 2A), especially in CC1-extended form (Figure 3E, right). Under a high salt condition (500 mM NaCl), CC1 adopted an extended form more frequently, which was quantified by the distance between the head and the gold labeled GFP (Figure 3D). This indicates that CC1a and CC1b electrostatically interact with each other. We propose that CC1 undergoes a large conformational change between the CC1-folded and CC1-extended forms and it is regulated by the intramolecular interaction within CC1, or between CAP-Gly and the proximal side of CC1 (Figure 3E).

The C-region of p150 is indispensable for the complex assembly

Our nanogold labeling demonstrated that p150 C-terminus was located at the middle of the shoulder (Figure 2B) and CC2-end at the base of the neck (Figure 2F), which suggested that the C-region of p150 constitutes a part of the shoulder (Figure 2H). The shoulder is thought to consist of p150, p50, and p24 subunits according to a previous biochemical analysis (Eckley *et al.*, 1999). Cryo-EM revealed that several α-helices were bundled in the shoulder, but no residues or peptides were assigned except the N-terminal domain of p50 extending along the Arp1 rod (Urnavicius *et al.*, 2015). Therefore, no structural data on localizations of p24 and the major portion of p50 in the dynactin complex are currently available. To clarify the organization of the shoulder domain, we next focused on p50, p24, and the C-region of p150.

The His-tag at the N-termini of p50 (p50-N-His) and p24 (p24-N-His) (Supplemental Figure S1[1]) were labeled and found to be localized close to the barbed end of the Arp1 rod (Figure 4A, top). The gold nanoparticles of both mutants exhibited similar distributions (Supplemental Figure S4[1A]) and they were closer to the barbed end than p150-C-His, being located at the intersection between the most proximal region in the sidearm and the Arp1 rod (Supplemental Figure S4[B]; Supplemental Table S2). For p50-C-His, the gold nanoparticles bound over a very broad area of the sidearm from the shoulder to the head (Figure 4A, bottom left) and an extraordinary form of the sidearm, without both the head and the neck domains, was occasionally observed (Supplemental Figure S4[1C]), suggesting that modification of p50 C-terminus impairs proper shoulder formation. p24-C-His exhibited typical sidearm morphology and the barbed end was labeled with gold nanoparticles (Figure 4A, bottom right). Collectively, these results confirm

FIGURE 2: Domain organization of p150. (A) Diagram of the p150 sequence divided into five regions: N-region, CC1, ICD, CC2, and C-region. The CAP-Gly domain (dark gray), CC1a (orange), CC1b (light blue), and CC2 (light green) are indicated. The arrows indicate the sites where a His-tag was inserted for nanogold labeling. (B) EM images of p150 mutant complexes (left, p150-N-His; right, p150-C-His) labeled with Ni-NTA gold nanoparticles (red arrowheads). The distribution of gold nanoparticles is shown in Supplemental Figure S2(1A and 1B) and Supplemental Table S2. (C) EM images of p150 CC1-start-His (top), p150 CC1-hinge-His (middle), and p150 CC1-end-His (bottom) labeled with gold nanoparticles (red arrowheads). Yellow arrows indicate the distal filament. (D) Top, the distribution of gold nanoparticles bound to p150 CC1-start-His (pink; $N = 82$), p150 CC1-hinge-His (yellow; $N = 41$), and p150 CC1-end-His (dark blue; $N = 110$). Bottom, the distance between the gold nanoparticle and the center of the head. Values (mean ± SD) are 10.9 ± 5.4 nm ($N = 82$), 22.2 ± 4.5 nm ($N = 41$), and 7.9 ± 3.3 nm ($N = 110$) for p150 CC1-start-His, p150 CC1-hinge-His, and p150 CC1-end-His, respectively. (E) Top, EM images of the CC1-deleted p150 (p150 ΔCC1) dynactin complex. Bottom, comparison of the lengths of the shoulder and the neck between the wild-type p150 (SBP-p62) and p150 ΔCC1. The lengths (mean ± SD) of the shoulder (Supplemental Figure S1[3F], the segment YZ) of SBP-p62 and of p150 ΔCC1 were 17.5 ± 3.3 nm ($N = 50$) and 15.9 ± 2.9 nm ($N = 40$), respectively. The lengths of the neck (Supplemental Figure S1[3F], the segment XY) of SBP-p62 and of p150 ΔCC1 were 17.7 ± 3.0 nm ($N = 50$) and 16.6 ± 2.8 nm ($N = 40$), respectively (two-sided Welch's *t* test, $p = 0.02$ for the shoulder and 0.06 for the neck). (F) EM images of p150 CC2-start-His (left) and p150 CC2-end-His (middle) labeled with gold nanoparticles (red arrowheads). The distribution of gold nanoparticles are shown in Supplemental Figure S2[1C and 1D] and Supplemental Table S2. EM images of p150 ΔCC2 (right). Yellow arrows indicate the distal filament formed by CC1. (G) EM images of p150 ΔICD (top left), p150 ΔICD-a (bottom left), p150 ΔICD-b (top right), and p135 (bottom right). Yellow arrows indicate the distal filament formed by CC1. Pink arrows indicate the head domain. See also Supplemental Figure S2(2B). (H) A summary of the folding pattern and the localization of p150 in the dynactin complex. Black crosses indicate the localization of the labeled sites in p150 mutants. The color codes are the same as those in A. Bars represent 20 nm.

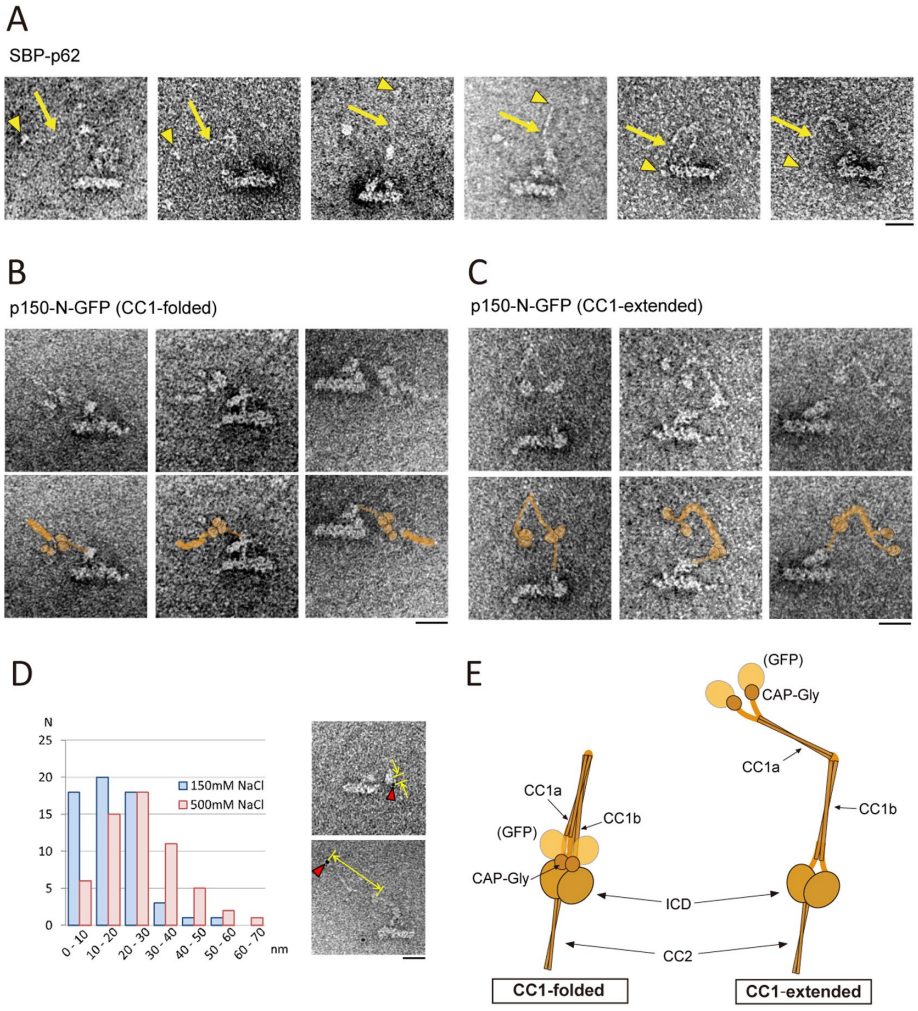

FIGURE 3: Conformational change of CC1. (A) EM images of SBP-p62 with longer CC1 (yellow arrows). Yellow arrowheads indicate the N-region at the tip of CC1. (B, C) Pairs of EM images of p150-N-GFP and the identical ones with the supposed location of p150 pseudocolored in orange. (B) ICD and GFP-N are in proximity at the bottom of CC1 (CC1-folded). (C) ICD and the GFP-N are observed as separate and distinguishable structures, these two domains being bridged by a hook-shaped CC1 (CC1-extended). (D) Conformation of CC1 in different salt concentrations. Left, histogram of the distance between the gold nanoparticle and the center of the head in 150 mM NaCl (light blue) and 500 mM NaCl (pink). Values are 17.3 ± 10.5 nm (N = 61) and 26.4 ± 12.8 nm (N = 58) (mean ± SD) for 150 and 500 mM NaCl, respectively. Right, representative images of gold-bound molecules in the CC1-folded form (top, 150 mM NaCl) and in the CC1-extended form (bottom, 500 mM NaCl). Red arrowheads indicate the gold nanoparticles and yellow arrows indicate the measured distance. (E) Schematic models for illustrating conformational change of CC1. The distal part of the sidearm (neck, head, and distal filament) is depicted. The domains in p150 (CAP-Gly, CC1a, CC1b, ICD, and CC2) and GFP are indicated. Left, CC1-folded form. Right, CC1-extended form. Bars represent 20 nm.

that p50 and p24 are situated in the shoulder domain and suggest that the C-terminus of p50 may have particular importance in shoulder formation and incorporation of p150 into the complex.

When the C-region of p150 was truncated (p150 ΔC in Supplemental Figure S1[1]), neither Arp1 nor p50 was copurified with this mutant (Supplemental Figure S1[2C]) and EM observation revealed that the Arp1 rod was not present and only a distal part of p150 (i.e., the sidearm without the shoulder) was found (Figure 4B). These results demonstrate that the C-region of p150 constitutes a part of the shoulder domain together with p50 and p24 and is indispensable for p150 incorporation into the dynactin complex. The importance of the C-region of p150 in complex formation might explain the *Glued*[1] mutation in fruit flies (McGrail *et al.*, 1995; Fan and Ready, 1997) where transcription of p150 is terminated in the middle of CC2 (Swaroop *et al.*, 1985). Furthermore, we found that isolated forms of p150/sidearm were frequently observed with the whole dynactin complex in the preparation of p150 mutants (Figure 4C). Because p150 is more abundant than other components in cells exogenously expressing recombinant p150 (Supplemental Figure S1[2C]), some p150 should exist as the isolated form not incorporated into the complex. The isolated p150 molecules with His-tags were confirmed to be labeled by gold nanoparticles (Supplemental Figure S4[1D]). Compared to the EM images of p150 ΔC (Figure 4B), the isolated p150/sidearm bore two additional oval structures (Figure 4C, left, pink arrow heads). These oval structures must be important for mediating p150 with the Arp1 rod and probably include p50 and p24 as well as the C-region of p150.

Morphological features and conformational change of the shoulder domain

To elucidate the morphological details of the shoulder domain in native sidearm, classes I and II (shoulder-undocked form) and class III (shoulder-docked form) obtained by single particle analysis (Supplemental Figure S1[4]) were further divided into subclasses (Supplemental Figure S5[1A]). The centroids of subclass averages of the shoulder domain in the shoulder-undocked form (classes I and II) were more distant from the Arp1 rod than in the shoulder-docked form (III) (Figure 5A, left). Besides, the undocked shoulders were more varied than the docked shoulders regarding their orientations and morphologies (Figure 5A, right; Supplemental Figure S5[1A]). On comparison of individual molecules in each subclass, the proximal side of the undocked shoulder was remarkably heterogeneous (Figure 5B; Supplemental Figure S5[1B]). This explains why the averaged images of the undocked shoulder appeared blurred and disconnected from the Arp1 rod (Figure 1C; Supplemental Figure S1[4]). Furthermore, the proximal shoulder was occasionally observed as two distinct filaments branching from the distal shoulder (red and light blue arrowheads in Figure 5B and Supplemental Figure S5[1C]). In these molecules, one filament pointed toward the center of the Arp1 rod (light blue arrowhead) and the other toward the end of the rod (red arrowhead). These structures probably correspond to Arm1 and Arm2, two symmetrical structures first visualized using cryo-EM (Urnavicius *et al.*, 2015). Meanwhile, both the distal and the proximal parts in the docked shoulder (class III in Figure 5, A and B) were highly homogenous, probably locating at their fixed positions alongside the Arp1 rod as in the previous studies (Chowdhury *et al.*, 2015; Urnavicius *et al.*, 2015). From these observations, we presume

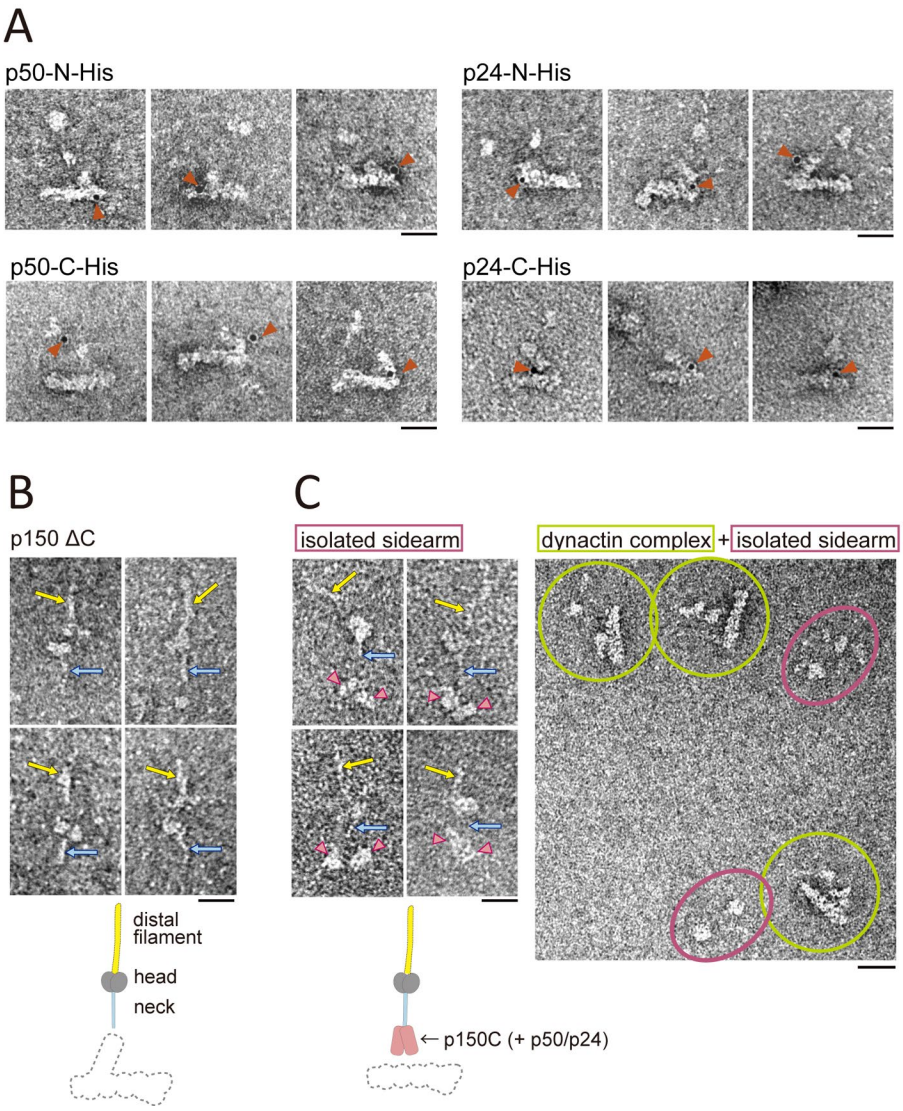

FIGURE 4: The shoulder domain is formed by p50, p24, and C-region of p150. (A) EM images of p50-N-His (top left), p50-C-His (bottom left), p24-N-His (top right), and p24-C-His (bottom right) labeled with gold nanoparticles (red arrowheads). See also Supplemental Figure S4(1). (B) EM images of p150 ΔC that lacks the C-region. The head, the distal filament formed by CC1 (yellow arrows) and the neck formed by CC2 (light blue arrows) are seen but the shoulder and the Arp1 rod are not (top), as illustrated in the cartoon (bottom). (C) Right, a general view of the EM image of a p150 mutant complex (p150-N-His). In addition to the dynactin complex (light green circles), isolated p150 particles (pink ellipses) are seen because the mutant p150 is more abundant than other subunits in cells exogenously expressing p150. Left, a gallery of EM images of isolated p150/sidearm (p150-N-His). Pink arrowheads indicate the proximal end of p150/sidearm, as illustrated in the cartoon (bottom). Bars represent 20 nm.

that Arm1, Arm2, and the Arp1 rod are tightly related to each other in the shoulder-docked form, whereas their interactions are partly weakened in the shoulder-undocked form.

To examine if dynactin exhibits transition between these shoulder forms, we changed salt concentrations in the solution. As a result, a higher salt concentration (200 mM KCl) increased the undocked forms and a lower salt concentration (100 mM KCl) increased the docked form (Figure 5C). Furthermore, with 100 mM KCl, a considerable number of molecules exhibited "sidearm-docked" form, which we define as the form where the neck crosses the Arp1 rod and the head position relative to the rod is fixed (Figure 5C, blue circles). The averaged image of the sidearm-docked form (Figure 5D, top right panel) resembled the cryo-EM image of dynactin complex reported previously (Urnavicius *et al.*, 2015). To quantify the ratio among the three sidearm conformations (shoulder undocked, shoulder docke,d and sidearm docked), particles obtained from different salt concentrations (100, 150, and 200 mM KCl) were classified using the common reference images (Figure 5D, top; Supplemental Figure S5[2A and 2B]). As shown in Figure 5D, bottom graphs, in 150 mM KCl, the ratio of the shoulder-undocked form was ~20%, that of the shoulder-docked form was ~60%, and that of the sidearm-docked form was ~20%. The shoulder-undocked form was more preferred in a higher salt concentration (200 mM KCl), probably because electrostatic interaction among the two arms and the Apr1 rod were weakened, whereas the sidearm-docked form was more preferred in a lower salt concentration (100 mM KCl) (Figure 5, Da–Dc). In our earlier experiments, the sidearm-docked form was rarely observed and the shoulder-undocked form was frequently observed (Figure 1; Supplemental Figure S1[4]), probably owing to its rather high salt condition (see *Materials and Methods*). Importantly, by subclassification of the shoulder-undocked particles in 200 mM KCl, the two arms in the proximal shoulder described earlier (Figure 5B) were observed in the averaged images (Supplemental Figure S5[2C]).

Subsequently, we repeatedly changed the salt concentration (150 mM–200 mM–150 mM). As a result, the conformation ratio depended mainly on the final condition (Figure 5Dd). In addition, glutaraldehyde crosslinking yielded increased sidearm-docked molecules and decreased shoulder-undocked molecules (Figure 5De). The salt concentration-changing experiment indicates that the sidearm reversibly transits among these conformations and the cross-linking experiment indicates that irreversible bond formations fix the sidearm on the Arp1 rod. Collectively, dynactin adopted all three shoulder/sidearm conformations in a certain ratio depending on the solution conditions and we reasoned that the equilibrium was determined by the strength of intramolecular interaction (Figure 5E).

DISCUSSION

Conformational diversity of sidearm and intramolecular interaction in dynactin complex

In this study, we investigated the molecular architecture of the dynactin complex by negative stain EM. Whereas the length and the thickness of the Arp1 rod were fairly constant, the sidearm was remarkably heterogeneous in its orientation and configuration (Figure 1). We explored the structure of the sidearm based on observation of individual molecules to visualize even the most flexible part of

the sidearm. Utilizing nanogold labeling and truncated mutants of the human dynactin complex, we revealed how p150 was folded and located within the distal side of the sidearm. Domain organization of p150 determined by our approach (Figure 2) is generally consistent with the proposed interpretation of the cryo-EM image of pig brain dynactin (Urnavicius *et al*., 2015). Both models markedly differ from the previous model (Schroer, 2004) especially in assignment of CC1 as the protrusion from the head and ICD as the head.

Although the cryo-EM study visualized the sidearm in a particular conformation (Urnavicius *et al*., 2015), our results indicated that it took on several characteristic conformations, implying that transitions and equilibrium between these conformations were regulated by intramolecular interactions in the dynactin complex (Figure 6) as follows. First, CC1 exhibited the extended and the folded forms (Figure 3). The previously reported interaction between CC1a and CC1b (Tripathy *et al*., 2014) must be important for CC1 to be folded (Figure 6, star 1). Second, the shoulder domain was either docked to or undocked from the Arp1 rod (Figures 1 and 5). When the shoulder was averaged in the docked form, we obtained a structure similar to those previously reported (Imai *et al*., 2006; Chowdhury *et al*., 2015; Urnavicius *et al*., 2015, 2018), suggesting the existence of the specific interactions between the shoulder and the Arp1 rod (Figure 6, star 2). Conversely, the undocked shoulder was highly heterogeneous (Figure 5, A and B) and the shoulder might be connected to the Arp1 rod in a different way (Supplemental Figure S6[2]). Finally, whereas the distal sidearm (neck, head, and distal filament) swept over wide areas even in the shoulder-docked form (Figure 1D), it was also observed to be fixed to the Arp1 rod in a certain population (10–30%, depending on salt concentrations or the existence of crosslinker) (Figure 5D). This sidearm-docked form closely resembles the cryo-EM image (Urnavicius *et al*., 2015) in which p150 CC1 and CC2 interact with the Arp1 rod (Figure 6, star 3 and star 4). Of note, the position of CC1 was fixed only in the presence of crosslinking agent, whereas CC2 seemed to be stably docked to the Arp1 rod in the absence of crosslinking agent (Supplemental Figure S5[2D and 2E]), suggesting CC1 would not always interact with the Arp1 rod even if CC2 and the head were docked to the rod. In summary, we propose that several distinct domains in the dynactin complex recognize each other and these intramolecular interactions enable dynactin to take on a broad spectrum of conformations as a complex (Supplemental Figure S6[1]). Since the conformations of CC1 and those of the sidearm were susceptible to salt concentrations (Figures 3D and 5D), electrostatic interactions play a key role. It is particularly important to determine currently unknown biological factors that trigger the conformational changes. We presume that association with other proteins such as MT, dynein, and cofactors (e.g., BICDs and HOOKs) may affect the preferable conformation.

Sidearm conformations in relation to dynactin functions

According to cryo-EM images (Urnavicius *et al*., 2015, 2018), the shoulder domain includes Arm1 (pointed side on the Arp1 rod) and Arm2 (barbed side), and they are identical in terms of their biochemical and structural components but highly asymmetric in their relationship to the Arp1 rod. The two arms in the undocked shoulder, investigated for the first time in this study, displayed another characteristic shape, resembling the letter "A" (Figure 5B; Supplemental Figure S5[2C]). Based on the facts that the ratio between the shoulder-docked form and the shoulder-undocked form reflected a slight change in the salt concentration (150–200 mM KCl) and that the transition between them was reversible (Figure 5, Db–Dd), it is likely that the interaction between the distal shoulder and the Arp1 rod (Figure 6, star 1) is weak and reversible, so we consider that dynactin shoulder adopts both the docked and the undocked forms (Supplemental Figure S6[2]). The interaction between dynactin and EM grid could also affect the orientation or the conformation of the protein, and therefore, it would be important to investigate the conformation of the shoulder domain in solution.

To date, functional roles of the shoulder domain have scarcely been explored. A recent study showed that the E53K mutation in Arp1 causes defects in fly oogenesis (Nieuwburg *et al*., 2017). Since the mutation site is located at the position where the shoulder and the Arp1 contact with each other, the interaction in the shoulder-docked form can be affected by the mutation. Intriguingly, in highly processive dynein-dynactin-BICD (HOOK) complex, dynactin adopted the shoulder-docked form (Chowdhury *et al*., 2015; Grotjahn *et al*., 2018; Urnavicius *et al*., 2015, 2018). Thus, one possibility is that the formation and/or maintenance of active dynein complex might require dynactin in the shoulder-docked form. On the other hand, we observed that the shoulder-undocked form was more flexible than the shoulder-docked form (Supplemental Figure S1[3C]; Figure 5, A and B). The undocked shoulder might enable dynactin to associate with dynein or MTs in more diverse ways.

Unlike the shoulder-docked form, CC1 and CC2 in p150 are docked to the Arp1 rod in the sidearm-docked form (Figure 6; Supplemental Figure S6[1]). Physiological roles of the sidearm-docked form are currently unknown. Pointed end of the Arp1 rod was suggested to interact with CC1 and regulate its function (Qiu *et al*., 2018). It is also possible that CC1 and CC2 compete with dynein or cofactors (BICDs or HOOKs) for Arp1 rod binding, inhibiting dynactin from forming an active dynein complex.

CC1 as a possible regulator for interaction with dynein and MT

There are some published descriptions of the dynein-binding sites within the CC1 region (Siglin *et al*., 2013; Tripathy *et al*., 2014). Moreover, binding of CC1 with dynein was shown to have both positive and negative effects on dynein motility, depending on the length of the fragment or the existence of adjacent domains (Tripathy *et al*., 2014; Kobayashi *et al*., 2017). Contrary to the well-known inhibitory effect of the CC1 fragment on dynein functions in cells (Quintyne *et al*., 1999) or in cell extract systems (Ishihara *et al*., 2014; Suzuki *et al*., 2017), its mechanism of action and in vitro effect on dynein motility remains controversial as described in the *Introduction*. In this study, we found that CC1 folded back at the CC1-hinge (Figure 2), and that CC1a and CC1b were in contact with each other (folded form) or were separated (extended form) (Figure 3). We speculate that the affinity of CC1 toward dynein IC and its apparently ambiguous effects on dynein motility are regulated by the conformational change of CC1. For example, an intramolecular interaction between CC1a and CC1b may regulate its effects on dynein, as proposed in the previous study (Tripathy *et al*., 2014). Moreover, it was recently discovered that the dynein tail interacted with the Arp1 rod with the aid of cofactors (Chowdhury *et al*., 2015; Urnavicius *et al*., 2015) and a functional relationship between this mode of interaction and the IC-CC1 based interaction is an open question.

In mammalian cells, the MT-binding property of the dynactin is controlled by expression of several isoforms in which alternative splicing affects the composition of the N-region (Dixit *et al*., 2008; Zhapparova *et al*., 2009). The p150 constructs used in this study (p150-B or DCTN1B) lacked exon 5–7 (basic amino acid-rich domain). Previously we examined the MT-binding ability of this isoform by TIRF microscopy and found that isolated p150-B rarely bound to MTs in vitro but that deletion of the CC1 domain remarkably restored the intrinsic MT-binding ability of CAP-Gly (Kobayashi *et al*., 2006, 2017).

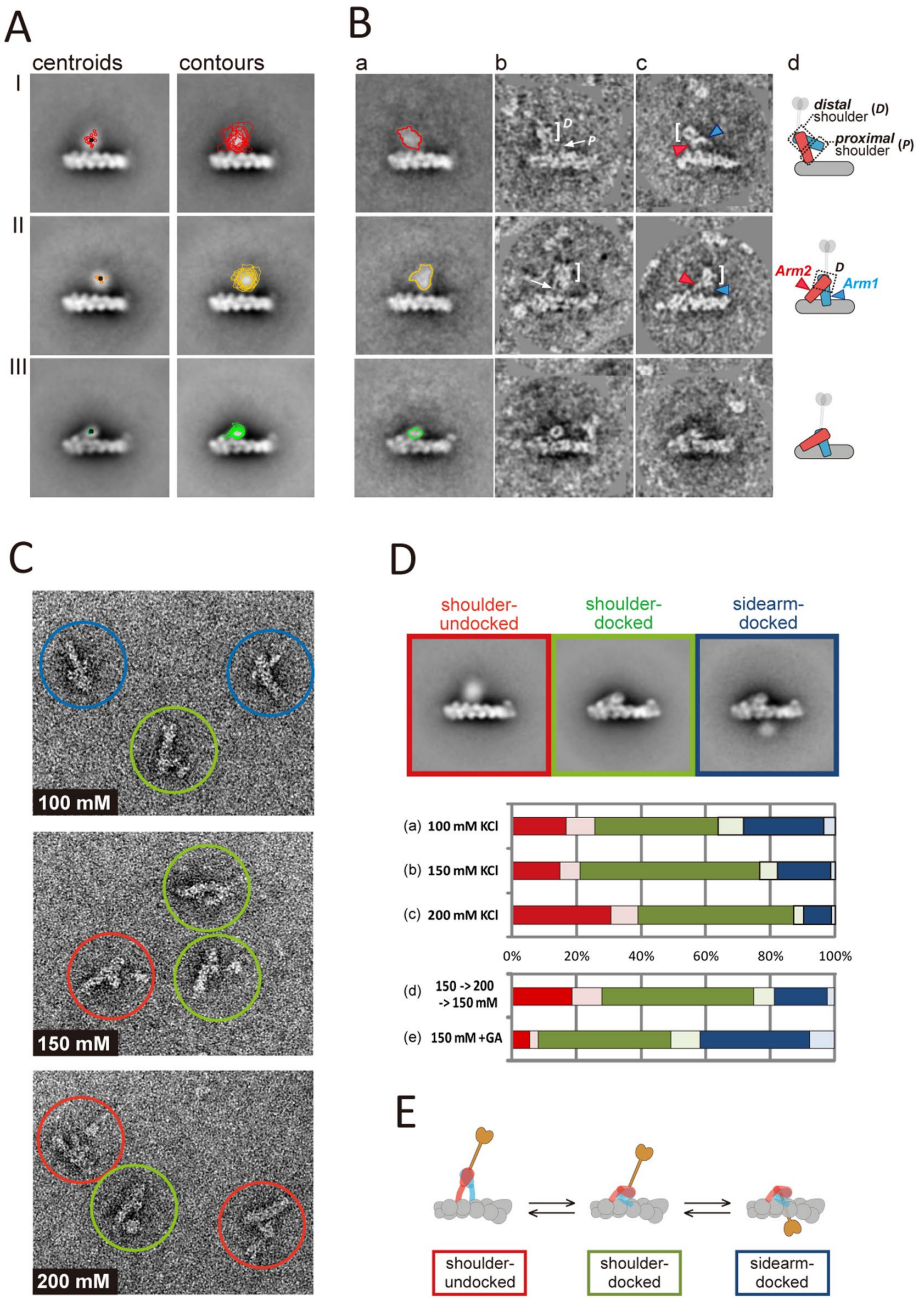

FIGURE 5: Morphological features of the shoulder domain and conformational changes of the sidearm. (A) Centroids and contour of the shoulder domains in subclasses of class I, II, and III (see Supplemental Figure S1[4]). Three classes of SBP-p62 were divided into 9–14 subclasses (Supplemental Figure S5[1A]). The shoulder domains in subclasses were detected by masking the Arp1 rod, and their centroids (left) and contour (right) are shown on the class averages in red (class I, $N = 12$), orange (class II, $N = 9$), and green (class III, $N = 12$). (B) Morphological characteristics of the shoulder domain. a, representative subclass averages (I-5, II-3, and III-1 in Supplemental Figure S5[1A]) with contoured shoulders. (b, c) Examples of aligned particles from each subclass stack (see Supplemental Figure S5[1B] for other examples). (d) Interpretations of the shoulder domain: distal shoulder (*D*, white brackets), proximal shoulder (*P*, white arrows), Arm1 (light blue arrowheads), and Arm2 (red arrowheads). See also Supplemental Figure S5(1C). (C) General views of SBP-p62 in varying concentrations of KCl (100, 150, and 200 mM). Molecules exhibiting the shoulder-undocked, the shoulder-docked, and the sidearm-docked forms are circled in red, green, and blue, respectively. (D) Top, the common reference images for classification of the sidearm forms. The averaged image of the shoulder-undocked (left), the shoulder-docked (middle), or the sidearm-docked (right) forms is generated from images with 200, 150, and 100 mM KCl, respectively. See Supplemental Figure S5(2A and 2B) for details. Bottom, the bar graphs representing the ratio of the three forms under each condition. The color codes (red, green, and blue) are the same as in C, with the lighter colors indicating misaligned particles. Particles were judged as misaligned when they had a low cross-correlation coefficient (<0.40) to the reference image. Solution conditions are as follows: 10 mM Pipes-K (pH 7.0) with 100 mM KCl (a), 150 mM KCl (b), or 200 mM KCl (c); (d) 10 mM Pipes-Na (pH 7.0) with 150 mM NaCl at first, 10 mM Pipes-K (pH 7.0) with 200 mM KCl in the middle, 10 mM Pipes-K (pH 7.0) with 150 mM KCl at last; (e) 10 mM Pipes-Na (pH 7.0) with 150 mM NaCl and fixed with final 0.5% glutaraldehyde for 15 min; $N = 2037$, 2036, 2699, 652, and 2039 for (a–e) in alphabetical order. (E) A model for conformational changes of the sidearm. The Arp1 rod (gray), Arm1 (light blue), Arm2 (red), and p150 (dark orange) are indicated. Note that the distal portion of the sidearm is not depicted here (see Figure 6 and Supplemental Figure S6[2]).

The conformational change of CC1 revealed by the present study offers a simple explanation for the difference in the MT-binding ability. In this model, the N-region including CAP-Gly is usually masked by the folded form of CC1 and this state inhibits the binding of the N-region to MTs; however, if the whole CC1 domain is deleted or CC1 is turned into the extended form, the N-region is unmasked and can bind to MTs. Structural basis for CAP-Gly/MT interaction has been explored using cryo-EM (Wang *et al.*, 2014) and solid state NMR (Yan *et al.*, 2015). Despite the flexible interaction of CAP-Gly with MTs (Wang *et al.*, 2014), a particular side of CAP-Gly, including the highly conserved GKNDG motif, was shown as the binding interface with MTs (Yan *et al.*, 2015). Since these structural data were obtained using the fragments of p150 without CC1, this surface might be covered with CC1 or ICD in the CC1-folded form as seen in Figure 3E, left.

Previous studies showed that the interaction between CAP-Gly and MTs was not always required for processive movement of dynein (Kardon *et al.*, 2009) but was necessary for the initiation of dynein-driven retrograde transport of vesicles from the neurite tip (Lloyd *et al.*, 2012; Moughamian and Holzbaur, 2012) and for the initiation of ultraprocessive movement of the dynein, dynactin, and BICD2 complex on tyrosinated MTs (McKenney *et al.*, 2016). Regulation of CAP-Gly by CC1 may be important for understanding these versatile effects of CAP-Gly on MT-based transport. In another cellular context, the regulation of dynactin MT-binding ability may play a key role in the passive transportation of dynein to the MT plus ends by +TIPs (Akhmanova and Steinmetz, 2008); that is, how dynein molecules

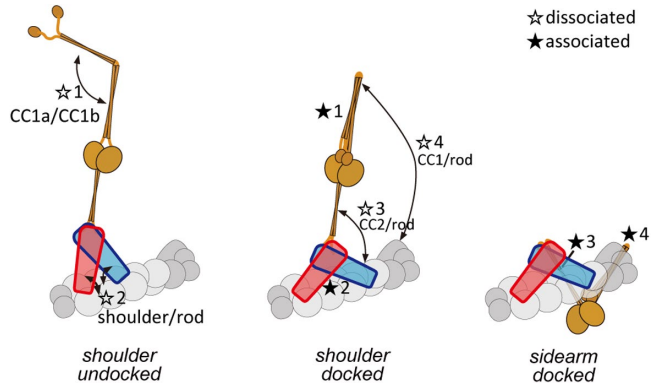

FIGURE 6: A model for conformational changes of dynactin complex. Gray, light blue, red, and dark orange domains indicate the Arp1 rod, Arm1, Arm2, and p150, respectively. Stars represent intramolecular interaction sites. The white and black stars indicate dissociated and associated forms, respectively. Left, a model of dynactin in the shoulder-undocked form, where the shoulder domain is dissociated from the Arp1 rod (star 2). CC1 is depicted in its extended form (star 1). Middle, a model of dynactin in the shoulder-docked form where the shoulder domain is associated with Arp1 rod. CC1 is depicted as in its folded form. Right, a model of dynactin in the sidearm docked form, where CC1 and CC2 are associated with the Arp1 rod (star 4 and 3, respectively). Although three conformations are shown here, seven conformations in total are proposed in our model (Supplemental Figure S6[1]). See Supplemental Figure S6(2) for a detailed structural model of the shoulder domain (Arm1 and Arm2).

are allotted to two pools of active motility and passive transportation examined in reconstitution assays (Baumbach *et al.*, 2017; Jha *et al.*, 2017) is possibly linked to the conformation of CC1.

This study reveals the conformational diversities of the entire sidearm and p150 CC1. High S/N ratio negative stain images and nanogold labeling revealed the flexible nature of the undocked sidearm, whereas single particle analysis confirmed the characteristic conformation of the docked sidearm. These findings reconcile the apparent inconsistency in configurations of the sidearm and CC1 in previous studies. Conformational diversity observed is likely to have functional significance. However, all the regulatory roles of the sidearm and CC1 proposed here are based on the premise that these conformational changes actually happen and are controlled in the cell. Thus, determination of the conformations in vivo, validation of the conformational transitions in vitro, and exploring structure–function relationships in particular conformations are the next important challenges.

MATERIALS AND METHODS

Construction of expression vectors

cDNAs encoding the dynactin subunits were amplified from HEK-293 cells by RT-PCR. The PCR primers used for cloning of dynactin subunits are as follows: 5′-ATGGCACAGAGCAAGAGGCAC-3′ and 5′-TTAGGAGATGAGGCGACTGTG-3′ for p150 (DCTN1, NM_004082), 5′-ATGGCGTCCTTGCTGCAGTCG-3′ and 5′-TTAAGGAAGAAGTGGGCCCAA-3′ for p62 (DYNC4, NM_001135643), 5′-ATGGCGGACCCTAAATACGCC-3′ and 5′-TCACTTTCCCAGCTTCTTCAT-3′ for p50 (DCTN2, NM_006400), and 5′-ATGGCGGGTCTGACTGACTTG-3′ and 5′-TCACTCCTCTGCTGGCTTCAC-3′ for p24 (DCTN3, NM_007234). Note that our cloned dynactin sample of p150 from HEK-293 cells was the DCTN1B isoform, which lacked some amino acids of the basic amino acid-rich domain (Δexon 5-7) as reported (Dixit *et al*, 2008; Zhapparova *et al*, 2009). We found a missense mutation (c.2566G>C) which produces p.A856T in the ICD region; however, we confirmed that the mutation does not affect the dynactin structure. The primers used for construction of p150 mutants are summarized in Supplemental Table S3. For p135 construction, N-terminal 131 amino acids were deleted and 17 amino acids were added to its N-terminus to mimic p135 isoform found in neuron (Tokito *et al*, 1996).

The PCR products were cloned into pcDNA5/FRT/TO (Life Technologies, Carlsbad, CA), a tetracycline-inducible mammalian expression vector. For protein purification, the SBP tag was fused at either the N- or C-terminus of the dynactin subunits. For Ni-NTA Au nanoparticle labeling, an octa-histidine tag (His-tag) was inserted in either the N- or C-terminus or internally through a short linker (Gly-Gly-Gly-Ser) (see Supplemental Figure S1[1]). The mutant p150-N-GFP has GFP fused at N-terminus of p150 as previously described (Kobayashi *et al.*, 2017). A His-tag and SBP tag were included in the GFP and used for purification (Kobayashi *et al.*, 2008). The insertion of these tags or deletion of specific domains was achieved by inverse PCR.

Generation of the stable HEK-293 cell lines for inducible expression of dynactin subunits

Flp-In T-REx HEK-293 cells (Life Technologies) were maintained in DMEM (Life Technologies) supplemented with 10% fetal calf serum and 2 mM L-glutamine. The stable cell lines for inducible expression of dynactin subunits were generated by cotransfection of the pcDNA5/FRT/TO vector containing recombinant dynactin subunits with the pOG44 vector encoding Flp recombinase according to the manufacturer's instructions. The transfectants were screened by including 100 μg/ml hygromycin, and the hygromycin-resistant colonies were harvested.

Purification of the dynactin complex

Purification of the dynactin complex was carried out using a SBP-tag (Ichikawa *et al*, 2011; Kobayashi and Murayama 2009). Stable HEK-293 cells were cultured in five 150-mm tissue culture dishes, and protein expression was induced by doxycycline (2 μg/ml) for 48 h. Cells were harvested, washed twice with phosphate-buffered saline, and homogenized in buffer A (50 mM Tris-HCl (pH 7.5), 0.15 M NaCl, 10% sucrose, 5 mM $MgSO_4$, and 1 mM dithiothreitol) containing 0.5 mM ATP, 0.05% Triton X-100, and complete mini protease inhibitor cocktail (Roche, Basel, Switzerland). The lysate was centrifuged and the resultant supernatant was applied onto a StrepTrap HP column (1 ml) (GE Healthcare, Chicago, IL) pre-equilibrated with buffer A. After extensive washing of the column with buffer A containing additional salt (final 0.5 M NaCl), the bound proteins were eluted in buffer A containing 2.5 mM desthiobiotin. The fraction from the peak of interest was quickly frozen in liquid nitrogen and stored at –80°C until use for EM observation.

SDS–PAGE and Western blotting

The purified dynactin complex was separated by SDS–PAGE using standard Laemmli's buffer system with 3–15% gradient gels and stained with Coomassie Brilliant Blue. For Western blotting, separated proteins were transferred onto PVDF membranes. The following antibodies were used for detection of dynactin subunits: p150 (Santa Cruz Biotechnology, sc-135890), p62 (Santa Cruz Biotechnology, sc-55604), p50 (BD Biosciences, 611002), Arp1 (Santa Cruz Biotechnology, sc-67321), Arp11 (Santa Cruz Biotechnology, sc-104807), CapZα (Santa Cruz Biotechnology, sc-1364391), CapZβ (Santa Cruz Biotechnology, sc-136502), p27 (Santa Cruz Biotechnology, sc-398694), p25 (Abnova, PAB23889), and p24 (Novus Biologicals, H00011258-B01P). Positive bands were

detected by chemiluminescence using HRP-labeled secondary antibodies.

Mass spectrometric analysis to identify proteins

Peptide mapping was carried out using the Triple TOF 5600 mass spectrometer systems consisting of nano-ESI and TOF (AB SCIEX MA, Framingham, MA). The Triple TOF 5600 mass spectrometer was combined with Eksigent NanoLC-Ultra system plus cHiPLC-nanoflex system (AB SCIEX MA, Framingham, MA) with attached 75 µm (id) × 15 cm Chrom XP C18-CL column. The solvent system consisted of (A) 0.1% formic acid/2% acetonitrile and (B) 0.1% formic acid/90% acetonitrile. The solvent was linearly increased from 2% B to 40% B for 40 min and subsequently kept at 90% B for 5 min. The flow rate was 300 nl/min. Identification of proteins was performed using Protein Pilot 4.0 software (AB SCIEX MA) (Hayashi *et al.*, 2013).

The proteins were subjected to digestion as described previously (Fujimura *et al.*, 2008). Finally, the residue was dissolved in 30 µl of 0.1% formic acid. Aliquots were used for peptide identification by mass spectrometry.

Negative stain EM, nanogold labeling, and image processing

For negative stain EM analysis, purified dynactin samples were diluted 4–5× in a buffer solution containing 10 mM Pipes-K (pH 7.0), 200 mM KCl, and 1 mM DTT. For the experiments shown in Figure 5, C and D and Supplemental Figure S5[2], the buffer solution of the purified samples was exchanged using Zeba Spin Desalting column (Thermo Fisher, Waltham, MA) for a buffer solution containing 10 mM Pipes-K (-Na) (pH 7.0), 100–200 mM KCl (NaCl), and 1 mM DTT. For the experiments presented in Figure 5De and Supplemental Figure S5[2F], the sample was mixed with final 0.5% glutaraldehyde for 15 min. Samples were not treated with glutaraldehyde in the other experiments. See Appendix 2 for a detailed examination of glutaraldehyde on the dynactin structure.

Samples were applied to prehydrophilized carbon-coated EM grids, negatively stained with 1.4% (wt/vol) uranyl acetate solution, and observed at 40,000× magnification in a transmission electron microscope, H7500 (Hitachi High-Techonologies, Tokyo, Japan) operating at 80 kV. Micrographs were taken using a 1024 × 1024 pixel CCD camera, Fast Scan-F114 (TVIPS, Gauting, Germany). Micrographs were taken at 40,000× and calibrated by catalase crystals, which gave a sampling of 2.6 Å/pixel at the object level. All experiments were performed independently at least twice. For each mutant, several EM grids were prepared and observed, and subsequently data were collected from the appropriately stained grids. The images were not inversed for the figure presentation, except panels a, k, and l in Figure 1.

Ni-NTA-gold nanoparticles were synthesized according to Kitai *et al.* (2011) using a modified method to reduce the diameter to 3 nm. The purified proteins were mixed with Ni-NTA-gold nanoparticles and incubated on ice for 30 min. The dynactin complex and Ni-NTA-gold nanoparticles were mixed to yield 10–20% labeled particles for all samples examined. These conditions were chosen to avoid nonspecific binding of Ni-NTA-gold nanoparticles. It is noted that the free Ni-NTA-gold nanoparticles rarely bound to the carbon surface of the grid, probably due to an electrostatic repulsion (see also Appendix 1 for specificity of nanogold labeling).

The length and angle in the EM images were measured using ImageJ software (National Institutes of Health). Reference points of dynactin (Supplemental Figure S1[3B]) and the center of the gold nanoparticles were determined by visual inspection. We used two different polar coordinates to measure and map these points (Supplemental Figure S1[3B, bottom]). For the gold nanoparticles bound around the head of dynactin, the distance from the origin (X: the center of the heads) and the angle from the neck direction (XY) were measured and mapped as shown in Supplemental Figure S1(3B, bottom, red coordinate). For the gold nanoparticles bound along the shoulder of dynactin and for the points within the sidearm, the distance from the origin (P: the barbed end of the Arp1 rod) and the angle from the Arp1 rod direction (PQ) were measured and mapped as shown in Supplemental Figure S1(3B, bottom, blue coordinate).

Images were processed using SPIDER software (Frank *et al.*, 1996). Dynactin complex particles were manually identified and picked using 280 × 280 pixel box and were low-pass filtered to 65 Å. Alignments and classifications of 2D negatively stained images were performed as described (Burgess *et al.*, 2004; Sladewski *et al.*, 2018). Initial global alignments were reference free, obtained by the SPIDER operations AP SR. Classifications were performed by K-means clustering. In the analyses in Figures 1–4; Supplemental Figure S1(S4); Figure 5, A and B; and Supplemental Figure S5(1), dynactin particles with distinctive sidearms were identified and analyzed as described in the legends to Supplemental Figure S1(4) and Figure 5, A and B. In the analyses in Figure 5D and Supplemental Figure S5(2), exploring the effect of solution conditions (salt or crosslinking agents) on sidearm conformations, all particles with the Arp1 rod were identified and analyzed as described in the legend to Figure 5D. Note that the former data set (Supplemental Figure S1[4]) were biased in that they contained more sidearm-undocked forms and less sidearm-docked forms than the latter data set (Supplemental Figure S5[2B]). Since the orientation of the dynactin particles on EM grids was rather constant in the shoulder-docked form and the sidearm-docked form but not in the shoulder-undocked form probably due to the interaction of dynactin with the carbon surface, the different image analyzing processes were taken for the different data sets as described above (see also Appendix 3).

ACKNOWLEDGMENTS

This work was supported by JSPS KAKENHI Grant Numbers 25117503 and 25291031 (to Y.Y.T.), 24590330 (to T.M.), 23300128 (to T.S.), and by MEXT-Supported Program for the Strategic Research Foundation at Private Universities, 2011-2015.

REFERENCES

Akhmanova A, Steinmetz MO (2008). Tracking the ends: a dynamic protein network controls the fate of microtubule tips. Nat Rev Mol Cell Biol 9, 309–322.

Ayloo S, Lazarus JE, Dodda A, Tokito M, Ostap EM, Holzbaur EL. (2014). Dynactin functions as both a dynamic tether and brake during dynein-driven motility. Nat Commun 5, 4807.

Baumbach J, Murthy A, McClintock MA, Dix CI, Zalyte R, Hoang HT, Bullock SL (2017). Lissencephaly-1 is a context-dependent regulator of the human dynein complex. Elife 6, e21768.

Burgess SA, Walker ML, Thirumurugan K, Trinick J, Knight PJ (2004). Use of negative stain and single-particle image processing to explore dynamic properties of flexible macromolecules. J Struct Biol 147, 247–258.

Carter AP, Diamant AG, Urnavicius L (2016). How dynein and dynactin transport cargos: a structural perspective. Curr Opin Struct Biol 37, 62–70.

Chowdhury S, Ketcham SA, Schroer TA, Lander GC (2015). Structural organization of the dynein-dynactin complex bound to microtubules. Nat Struct Mol Biol 22, 345–347.

Cianfrocco MA, DeSantis ME, Leschziner AE, Reck-Peterson SL (2015). Mechanism and regulation of cytoplasmic dynein. Annu Rev Cell Dev Biol 31, 83–108.

Culver-Hanlon TL, Lex SA, Stephens AD, Quintyne NJ, King SJ (2006). A microtubule-binding domain in dynactin increases dynein processivity by skating along microtubules. Nat Cell Biol 8, 264–270.

Dixit R, Levy JR, Tokito M, Ligon LA, Holzbaur EL (2008). Regulation of dynactin through the differential expression of p150Glued isoforms. J Biol Chem 283, 33611–33619.
Echeverri CJ, Paschal BM, Vaughan KT, Vallee RB (1996). Molecular characterization of the 50-kD subunit of dynactin reveals function for the complex in chromosome alignment and spindle organization during mitosis. J Cell Biol 132, 617–633.
Eckley DM, Gill SR, Melkonian KA, Bingham JB, Goodson HV, Heuser JE, Schroer TA (1999). Analysis of dynactin subcomplexes reveals a novel actin-related protein associated with the arp1 minifilament pointed end. J Cell Biol 147, 307–320.
Fan SS, Ready DF (1997). Glued participates in distinct microtubule-based activities in Drosophila eye development. Development 124, 1497–1507.
Frank J, Radermacher M, Penczek P, Zhu J, Li Y, Ladjadj M, Leith A (1996). SPIDER and WEB: processing and visualization of images in 3D electron microscopy and related fields. J Struct Biol 116, 190–199.
Fujimura T, Shinohara Y, Tissot B, Pang PC, Kurogochi M, Saito S, Arai Y, Sadilek M, Murayama K, Dell A, *et al.* (2008). Glycosylation status of haptoglobin in sera of patients with prostate cancer vs. benign prostate disease or normal subjects. Int J Cancer 122, 39–49.
Grotjahn DA, Chowdhury S, Xu Y, McKenney RJ, Schroer TA, Lander GC (2018). Cryo-electron tomography reveals that dynactin recruits a team of dyneins for processive motility. Nat Struct Mol Biol 25, 203–207.
Guo C, Williams JC, Polenova T (2019). Conformational flexibility of p150Glued(1-191) subunit of dynactin assembled with microtubules. Biophys J 117, 938–949.
Hayashi T, Saito T, Fujimura T, Hara K, Takamochi K, Mitani K, Mineki R, Kazuno S, Oh S, Ueno T, *et al.* (2013). Galectin-4, a novel predictor for lymph node metastasis in lung adenocarcinoma. PLoS One 8, e81883.
Hodgkinson JL, Peters C, Kuznetsov SA, Steffen W (2005). Three-dimensional reconstruction of the dynactin complex by single-particle image analysis. Proc Natl Acad Sci USA 102, 3667–3672.
Ichikawa M, Watanabe Y, Murayama T, Toyoshima YY (2011). Recombinant human cytoplasmic dynein heavy chain 1 and 2: observation of dynein-2 motor activity in vitro. FEBS Lett 585, 2419–2423.
Imai H, Narita A, Maéda Y, Schroer TA (2014). Dynactin 3D structure: implications for assembly and dynein binding. J Mol Biol 426, 3262–3271.
Imai H, Narita A, Schroer TA, Maeda Y (2006). Two-dimensional averaged images of the dynactin complex revealed by single particle analysis. J Mol Biol 359, 833–839.
Ishihara K, Nguyen PA, Groen AC, Field CM, Mitchison TJ (2014). Microtubule nucleation remote from centrosomes may explain how asters span large cells. Proc Natl Acad Sci USA 111, 17715–17722.
Jacquot G, Maidou-Peindara P, Benichou S (2010). Molecular and functional basis for the scaffolding role of the p50/dynamitin subunit of the microtubule-associated dynactin complex. J Biol Chem 285, 23019–23031.
Jha R, Roostalu J, Cade NI, Trokter M, Surrey T (2017). Combinatorial regulation of the balance between dynein microtubule end accumulation and initiation of directed motility. EMBO J 36, 3387–3404.
Kardon JR, Reck-Peterson SL, Vale RD (2009). Regulation of the processivity and intracellular localization of Saccharomyces cerevisiae dynein by dynactin. Proc Natl Acad Sci USA 106, 5669–5674.
Kardon JR, Vale RD (2009). Regulators of the cytoplasmic dynein motor. Nat Rev Mol Cell Biol 10, 854–865.
Karki S, Holzbaur EL (1995). Affinity chromatography demonstrates a direct binding between cytoplasmic dynein and the dynactin complex. J Biol Chem 270, 28806–28811.
King SJ, Brown CL, Maier KC, Quintyne NJ, Schroer TA (2003). Analysis of the dynein-dynactin interaction in vitro and in vivo. Mol Biol Cell 14, 5089–5097.
Kitai T, Watanabe Y, Toyoshima YY, Kobayashi T, Murayama T, Sakaue H, Suzuki H, Takahagi T (2011). Simple method of synthesizing nickel—nitrilotriacetic acid gold nanoparticles with a narrow size distribution for protein labeling. Jpn J Appl Phys 50, 095002–095005. http://dx.doi.org/10.1143/JJAP.50.095002.
Kobayashi T, Miyashita T, Murayama T, Toyoshima YY (2017). Dynactin has two antagonistic regulatory domains and exerts opposing effects on dynein motility. PLoS One 12, e0183672.
Kobayashi T, Morone N, Kashiyama T, Oyamada H, Kurebayashi N, Murayama T (2008). Engineering a novel multifunctional green fluorescent protein tag for a wide variety of protein research. PLoS One 3, e3822.
Kobayashi T, Murayama T (2009). Cell cycle-dependent microtubule-based dynamic transport of cytoplasmic dynein in mammalian cells. PLoS One 4, e7827.
Kobayashi T, Shiroguchi K, Edamatsu M, Toyoshima YY (2006). Microtubule-binding properties of dynactin p150 expedient for dynein motility. Biochem Biophys Res Commun 340, 23–28.
Konno T, Ross OA, Teive HAG, Sławek J, Dickson DW, Wszolek ZK (2017). DCTN1-related neurodegeneration: Perry syndrome and beyond. Parkinsonism Relat Disord 41, 14–24.
Lloyd TE, Machamer J, O'Hara K, Kim JH, Collins SE, Wong MY, Sahin B, Imlach W, Yang Y, Levitan ES, *et al.* (2012). The p150(Glued) CAP-Gly domain regulates initiation of retrograde transport at synaptic termini. Neuron 74, 344–360.
Maier KC, Godfrey JE, Echeverri CJ, Cheong FK, Schroer TA (2008). Dynamitin mutagenesis reveals protein-protein interactions important for dynactin structure. Traffic 9, 481–491.
Mcgrail M, Gepner J, Silvanovich A, Ludmann S, Serr M, Hays TS (1995). Regulation of cytoplasmic dynein function in vivo by the Drosophila glued complex. J. Cell Biol 131, 411–425.
McKenney RJ, Huynh W, Vale RD, Sirajuddin M (2016). Tyrosination of α-tubulin controls the initiation of processive dynein-dynactin motility. EMBO J 35, 1175–1185.
Melkonian KA, Maier KC, Godfrey JE, Rodgers M, Schroer TA (2007). Mechanism of dynamitin-mediated disruption of dynactin. J Biol Chem 282, 19355–19364.
Miura M, Matsubara A, Kobayashi T, Edamatsu M, Toyoshima YY (2010). Nucleotide-dependent behavior of single molecules of cytoplasmic dynein on microtubules in vitro. FEBS Lett 584, 2351–2355.
Morgan JL, Song Y, Barbar E (2011). Structural dynamics and multiregion interactions in dynein-dynactin recognition. J Biol Chem 286, 39349–39359.
Moughamian AJ, Holzbaur EL (2012). Dynactin is required for transport initiation from the distal axon. Neuron 74, 331–343.
Nieuwburg R, Nashchekin D, Jakobs M, Carter AP, Khuc Trong P, Goldstein RE, St Johnston D (2017). Localised dynactin protects growing microtubules to deliver oskar mRNA to the posterior cortex of the Drosophila oocyte. Elife 6, e27237.
Qiu R, Zhang J, Xiang X (2018). p25 of the dynactin complex plays a dual role in cargo binding and dynactin regulation. J Biol Chem 293, 15606–15619.
Quintyne NJ, Gill SR, Eckley DM, Crego CL, Compton DA, Schroer TA (1999). Dynactin is required for microtubule anchoring at centrosomes. J Cell Biol 147, 321–334.
Schafer DA, Gill SR, Cooper JA, Heuser JE, Schroer TA (1994). Ultrastructural analysis of the dynactin complex: an actin-related protein is a component of a filament that resembles F-actin. J Cell Biol 126, 403–412.
Schroer TA (2004). Dynactin. Annu Rev Cell Dev Biol 20, 759–779.
Siglin AE, Sun S, Moore JK, Tan S, Poenie M, Lear JD, Polenova T, Cooper JA, Williams JC (2013). Dynein and dynactin leverage their bivalent character to form a high-affinity interaction. PLoS One 8, e59453.
Sladewski TE, Billington N, Ali MY, Bookwalter CS, Lu H, Krementsova EB, Schroer TA, Trybus KM (2018). Recruitment of two dyneins to an mRNA-dependent Bicaudal D transport complex. Elife 26, 7.
Steinmetz MO, Akhmanova A (2008). Capturing protein tails by CAP-Gly domains. Trends Biochem Sci 33, 535–545.
Suzuki K, Miyazaki M, Takagi J, Itabashi T, Ishiwata S (2017). Spatial confinement of active microtubule networks induces large-scale rotational cytoplasmic flow. Proc Natl Acad Sci USA 114, 2922–2927.
Swaroop A, Paco-Larson ML, Garen A (1985). Molecular genetics of a transposon-induced dominant mutation in the Drosophila locus Glued. Proc Natl Acad Sci USA 82, 1751–1755.
Tokito MK, Howland DS, Lee VM, Holzbaur EL (1996). Functionally distinct isoforms of dynactin are expressed in human neurons. Mol Biol Cell 7, 1167–1180.
Tripathy SK, Weil SJ, Chen C, Anand P, Vallee RB, Gross SP (2014). Autoregulatory mechanism for dynactin control of processive and diffusive dynein transport. Nat Cell Biol 16, 1192–1201.
Urnavicius L, Lau CK, Elshenawy MM, Morales-Rios E, Motz C, Yildiz A, Carter AP (2018). Cryo-EM shows how dynactin recruits two dyneins for faster movement. Nature 554, 202–206.
Urnavicius L, Zhang K, Diamant AG, Motz C, Schlager MA, Yu M, Patel NA, Robinson CV, Carter AP (2015). The structure of the dynactin complex and its interaction with dynein. Science 347, 1441–1446.
Vaughan KT, Vallee RB (1995). Cytoplasmic dynein binds dynactin through a direct interaction between the intermediate chains and p150Glued. J Cell Biol 131(6 Pt 1), 1507–1516.
Waterman-Storer CM, Karki S, Holzbaur EL (1995). The p150Glued component of the dynactin complex binds to both microtubules and the

actin-related protein centractin (Arp-1). Proc Natl Acad Sci USA 92, 1634–1638.
Yan S, Guo C, Hou G, Zhang H, Lu X, Williams JC, Polenova T (2015). Atomic-resolution structure of the CAP-Gly domain of dynactin on polymeric microtubules determined by magic angle spinning NMR spectroscopy. Proc Natl Acad Sci USA 112, 14611–14616
Yeh TY, Kowalska AK, Scipioni BR, Cheong FK, Zheng M, Derewenda U, Derewenda ZS, Schroer TA (2013). Dynactin helps target Polo-like kinase 1 to kinetochores via its left-handed beta-helical p27 subunit. EMBO J 32, 1023–1035.
Yeh TY, Quintyne NJ, Scipioni BR, Eckley DM, Schroer TA (2012). Dynactin's pointed-end complex is a cargo-targeting module. Mol Biol Cell 23, 3827–3837.
Zhang J, Yao X, Fischer L, Abenza JF, Peñalva MA, Xiang X (2011). The p25 subunit of the dynactin complex is required for dynein-early endosome interaction. J Cell Biol 193, 1245–1255.
Zhapparova ON, Bryantseva SA, Dergunova LV, Raevskaya NM, Burakov AV, Bantysh OB, Shanina NA, Nadezhdina ES (2009). Dynactin subunit p150Glued isoforms notable for differential interaction with microtubules. Traffic 10, 1635–1646.